Center vortex structure in the presence of dynamical fermions

James C. Biddle, Waseem Kamleh, and Derek B. Leinweber

Centre for the Subatomic Structure of Matter, Department of Physics, The University of Adelaide,
South Australia 5005, Australia

An analysis of the geometry and structure of center vortices in the presence of dynamical fermions is performed. A variety of metrics are used to measure the matrix structure of the vortex-modified gauge fields. Visualizations of center vortices are presented and percolating clusters are identified. The size of secondary vortex clusters is analyzed, with substantial differences observed between the pure Yang-Mills and dynamical fermion case. Vortex fields are represented as directed graphs, with branching points acting as the vertices. This representation leads to a novel picture of vortex branching as a binomial process. These results elucidate the change in the center vortex vacuum induced by the introduction of dynamical fermions.

I. INTRODUCTION

There is now a wealth of literature exploring the impact of center vortices on pure Yang-Mills gauge theory [1–26]. These results have consistently shown that center vortices play an important role in the emergence of nonperturbative properties. However, there have also been consistent discrepancies between original and vortex-only calculations. Recent results [27,28] have, for the first time, considered center vortices in the presence of dynamical fermions. These results demonstrated the dramatic effect dynamical fermions have on the behavior of center vortices. In contrast to prior pure Yang-Mills studies [19,21,22,25,29–31], the static quark potential can be fully recreated from center vortices alone [27], and vortex removal results in complete suppression of the infrared Landau-gauge gluon propagator [28]. In light of these unexpected results, it is natural seek a deeper understanding of these effects by directly analyzing the structure of the vortices themselves.

In this work, we first look for changes in the bulk properties of the lattice configurations by analyzing the norms and traces of the gauge links, as well as the values of the maximal center gauge functional. Bulk discrepancies between pure-gauge and dynamical ensembles may suggest where the differences in vortex structure arise from.

We then expand upon the visualization techniques developed in Ref. [32] to analyze the geometric structure of center vortices. New developments allow us to split the vortex structure into individual disconnected clusters. From these clusters we may examine the degree of vortex percolation present in the vacuum.

In the supplemental material located at [33], visualizations of these center vortex clusters are presented as interactive 3D models embedded in the document. Instructions on viewing these models are also included therein. Figures with a corresponding interactive model that can be found in the supplemental material are marked as *Interactive* in the caption. Interactive models in the Supplementary Material are also referenced as Figs. S-x in the text. A selection of preset views that highlight regions of interest is also available.

Following cluster identification, we present a novel perspective that considers each cluster as a directed graph of vortex branching points, with the weight of each graph edge corresponding to the number of vortex plaquettes between branching points. This data structure enables us to develop quantitative measures of the size and shape of center vortex clusters, facilitating a detailed comparison of vortex structure between pure-gauge and dynamical QCD.

This paper is structured as follows. In Sec. II we detail the center vortex model and how center vortices are identified on the lattice. We then present the analysis of the bulk gauge-link properties in Sec. III. In Sec. IV our visualization conventions are introduced. In Sec. V we discuss the cluster identification algorithm and subsequent findings. In Sec. VI we introduce the method by which vortex clusters can be converted to a graph, and discuss the analysis performed on these graphs. Finally, the findings of this work are summarized in Sec. VII.

II. CENTER VORTICES

In QCD, center vortices are regions of a gauge field that carry flux associated with $\mathbb{Z}_3$, the center of the $SU(3)$ gauge group. $\mathbb{Z}_3$ consists of the three elements,

$$\mathbb{Z}_3 = \left\{ \exp\left(m\frac{2\pi i}{3} \right) I, m = -1, 0, +1 \right\}. \quad (1)$$

For the purposes of our discussion, m will be referred to as the center charge of the vortex. On the lattice, thin center vortices appear as closed sheets in four dimensions, or as closed lines on three-dimensional slices of the lattice.

Center vortices are identified on the lattice through a well-known procedure [32,34], briefly summarized here. First, the configurations are rotated to the maximal center gauge (MCG) by determining a gauge rotation, $\Omega(x)$, that maximizes the functional [23,31,34]

$$\Phi = \frac{1}{VN_{\text{dim}}n_c^2} \sum_{x,\mu} |\text{Tr}U_\mu^\Omega(x)|^2. \quad (2)$$

This process brings each gauge link as close as possible to one of the elements of $\mathbb{Z}_3$. Once the ensemble has been fixed to maximal center gauge, each link is projected onto the nearest center element, $U_\mu(x) \to Z_\mu(x)$, as defined by the phase of the trace of each link. Center vortices are then identified by the location of nontrivial plaquettes $P_{\mu\nu} = \exp(m\frac{2\pi i}{3})I$, in the μ-ν plane with $m = \pm 1$. This process of center projection defines the vortex-only ensemble, $Z_\mu(x)$. Using these identified vortices, we also construct the vortex-removed ensemble by computing $R_\mu(x) = Z_\mu^\dagger(x)U_\mu(x)$. Hence, this procedure results in three ensembles:

(1) Original, untouched (UT) fields, $U_\mu(x)$,
(2) Vortex-only (VO) fields, $Z_\mu(x)$,
(3) Vortex-removed (VR) fields, $R_\mu(x)$,

Visualizations of vortices are naturally constructed from the vortex-only ensembles, and as such the $Z_\mu(x)$ fields will be of primary focus in this work. However, the effectiveness of vortex removal is also of great interest as it has been observed that the vortex removed ensembles also vary in behavior depending on the presence or absence of dynamical fermions [27,28].

For this work, we continue the analysis performed in our previous work [27,28] and make use of three original (UT) ensembles. Each ensemble has dimensions $32^3 \times 64$ and is comprised of 200 lattice configurations. Two of the ensembles are $(2+1)$-flavor dynamical ensembles from the PACS-CS Collaboration [35]. We choose the heaviest and lightest pion mass ensembles, with masses of 701 MeV and 156 MeV, respectively. This allows us to observe the greatest differentiation between the dynamical ensembles. The third ensemble is pure Yang-Mills, generated with the Iwasaki gauge action [36]. The lattice spacing is tuned to be

TABLE I. A summary of the lattice ensembles used in this work [35].

Type	a (fm)	β	$\kappa_{\text{u,d}}$	m_π (MeV)
Pure gauge	0.100	2.58	$\cdots$	$\cdots$
Dynamical	0.102	1.9	0.13700	701
Dynamical	0.093	1.9	0.13781	156

similar to that of the PACS-CS ensembles. A summary of the lattice parameters is provided in Table I.

III. BULK PROPERTIES

In understanding the impact dynamical fermions have on the center-vortex vacuum, it is natural to first look for bulk changes in the $SU(3)$ lattice gauge fields upon the introduction of dynamical fermions. The first measure we examine is the distribution of the local MCG functional

$$\phi_\mu(x) = \frac{1}{n_c^2} |\text{Tr}U_\mu^\Omega(x)|^2 \quad (3)$$

defined such that the total MCG functional given in Eq. (2) can be written as

$$\Phi = \frac{1}{VN_{\text{dim}}} \sum_{x,\mu} \phi_\mu(x) \quad (4)$$

The distribution of $R_\mu(x)$ values is presented for the untouched ensembles in Fig. 1.

We observe that the pure gauge ensemble achieves a typically larger value of $\phi_\mu(x)$, indicating that the links have been brought closer to the center of $SU(3)$. The two dynamical ensembles follow each other rather closely, although the heavier pion mass appears to achieve slightly larger Φ values than its lighter counterpart. It should be
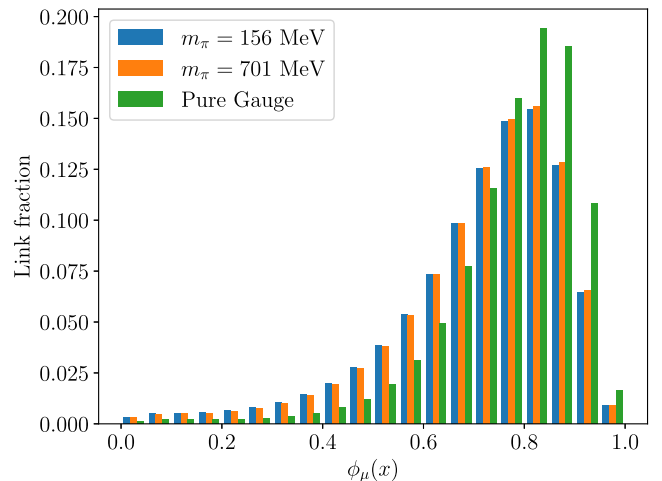
FIG. 1. Distribution of the local maximal center gauge functional, $R_\mu(x)$, as defined in Eq. (3).
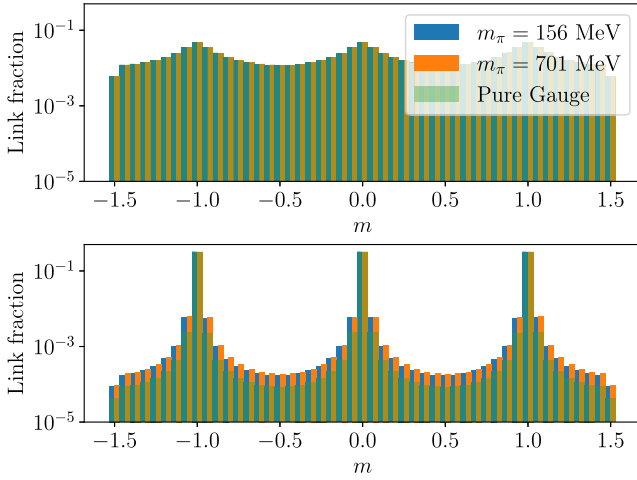
FIG. 2. Distribution of trace phases before (*top*) and after (*bottom*) fixing to MCG. We plot the bins for the dynamical ensembles side-by-side as they are similar to one another, with the pure gauge results overlayed.

FIG. 3. Distribution of trace magnitudes before (*top*) and after (*bottom*) fixing to MCG.

noted however that larger values of $\phi_\mu(x)$ do not necessarily indicate that the MCG algorithm has performed better on these ensembles. As was determined in Refs. [19,37,38], there are a number of methods that can be used to increase the typical values of $\phi_\mu(x)$ obtained from maximal center gauge. However, these methods do not necessarily improve the vortex-finding abilities of the procedure and in some cases actually degrade the vortex-finding performance. As such, it should be understood that the results presented in Fig. 1 are simply showing a noticeable change in behavior as we transition from pure gauge to dynamical ensembles, and not necessarily a worsening of vortex identification.

Next, we wish to compare the distribution of the trace phases, $\arg\left(\mathrm{Tr}\,U_\mu(x)\right)$, from each ensemble both before and after fixing to maximal center gauge. These results are presented in Fig. 2. As intended, the phases are tightly packed about the three center values after fixing to maximal center gauge. However, the pure-gauge results are distributed slightly closer to the center elements than the dynamical ensembles.

In conjunction with the trace phases, we can also look at the magnitude of the traces, $|\mathrm{Tr}\,U_\mu(x)|$. These values are presented in Fig. 3. Note that a center element will have $|\mathrm{Tr}\,U_\mu(x)| = 3$. MCG then clearly serves to not only bring the phases close to that of a center element, but also the magnitude. However, the effect on the magnitude is less than that on the phase. This suggests that there is still significant off-diagonal strength in the original ensembles after fixing to maximal center gauge. Again, the pure gauge values are distributed closer to the center value of three when compared with the dynamical results.

The next bulk measures we examine are two matrix norms designed to determine the residual off-diagonal
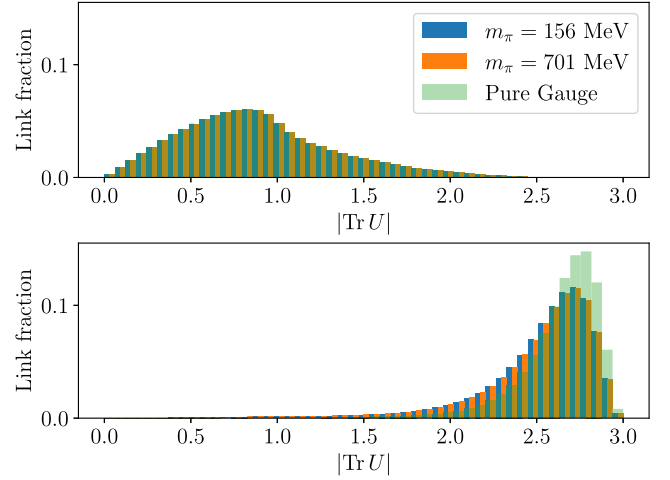
strength present in the vortex-removed fields in MCG. The norms are

$$L_\mu(x) = \left(\sum_{i,j} |U_\mu^{ij}(x) - \delta_{ij}|^2\right)^{\frac{1}{2}}, \tag{5}$$

and

$$M_\mu(x) = \left(\sum_{\substack{i,j \\ i \neq j}} |U_\mu^{ij}(x)|^2\right)^{\frac{1}{2}}, \tag{6}$$

where i, j denote the $SU(3)$ color indices. We find for the untouched configurations that the results for both norms are identical across all ensembles, as shown in Figs. 4 and 5. However, after vortex removal we notice that differences appear in both norms. The results for $L_\mu(x)$ and $M_\mu(x)$ on the vortex removed ensembles are shown in Figs. 6 and 7, respectively.
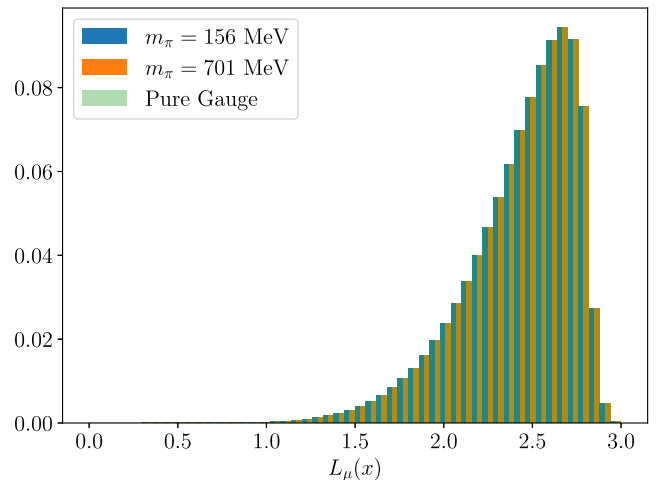
FIG. 4. The $L_\mu(x)$ norm calculated prior to fixing to MCG.
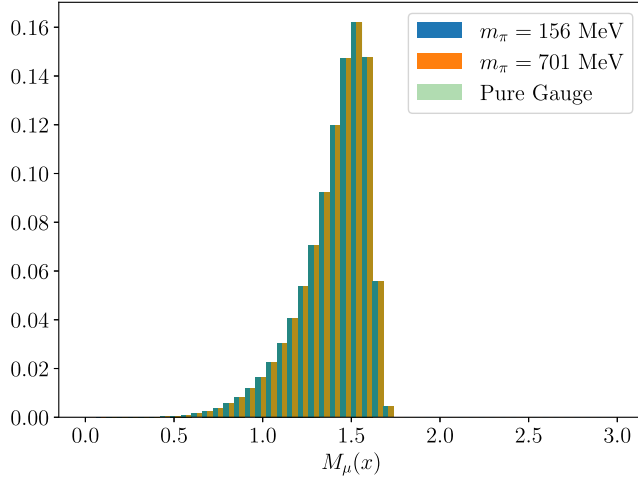
FIG. 5. The $M_\mu(x)$ norm calculated prior to fixing to MCG.
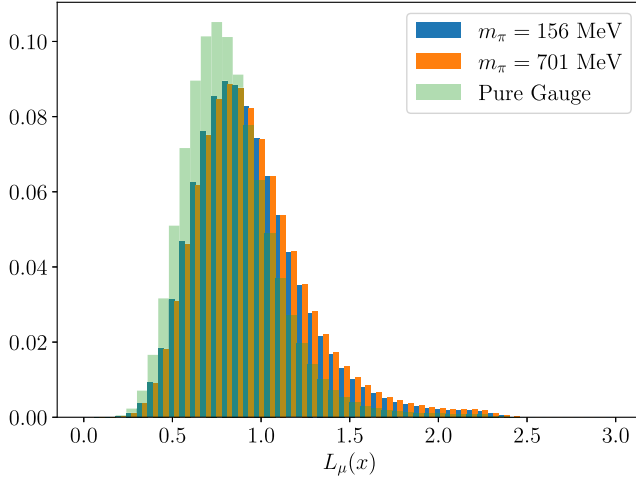
FIG. 6. The $L_\mu(x)$ norm calculated on the VR ensembles. Here we see the change in behavior after the introduction of dynamical fermions.
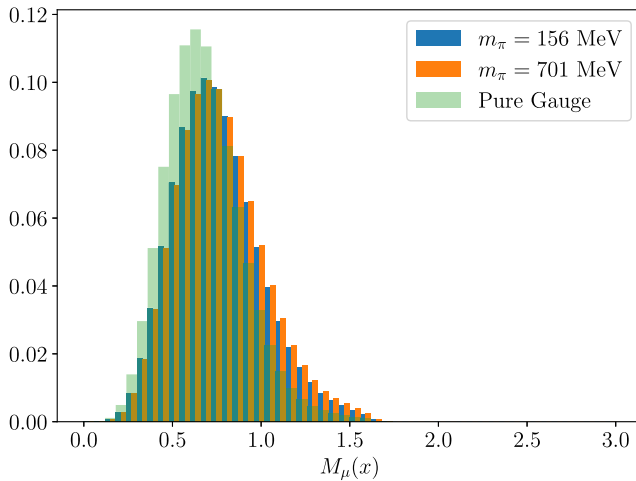
FIG. 7. The $M_\mu(x)$ norm calculated on the VR ensembles. A trend similar to that seen in Fig. 6 is observed.

We observe that the dynamical ensembles retain a greater proportion of their off-diagonal strength. This is interesting, as it has been shown in Ref. [28] that vortex removal results in a more significant loss of infrared strength in the Landau-gauge gluon propagator when dynamical fermions are present. This indicates that the residual strength as measured by our norms in MCG does not coincide with enhancement as measured via the Landau-gauge gluon propagator.

These measures indicate that there is a substantial difference in behavior between the pure-gauge and dynamical ensembles when considering their MCG matrix substructure. Both the trace phases and magnitudes are further from the center elements and the dynamical ensembles retain more off-diagonal strength.

IV. VISUALIZATIONS

Motivated by the difference in the bulk structure of the gauge fields in maximal center gauge, we now wish to look more closely at the fine-grained structure of the vortex vacuum. We do this by extending the visualization techniques first developed in Ref. [32]. Given that vortices are associated with nontrivial plaquettes, vortices themselves exist on the dual lattice. Hence, for a vortex-only ensemble we write the plaquette as [15,26]

$$P_{\mu\nu}(x) = \exp\left(\frac{\pi i}{3}\epsilon_{\mu\nu\kappa\lambda}m_{\kappa\lambda}(\bar{x})\right), \qquad (7)$$

where $m_{\kappa\lambda}(\bar{x}) \in \{-1, 0, 1\}$ defines the directed vortex charge orthogonal to the plaquette and based at $\bar{x} = x + \frac{a}{2}(\hat{\mu} + \hat{\nu} - \hat{\kappa} - \hat{\lambda})$. Note also that $m_{\kappa\lambda}(\bar{x})$ is antisymmetric under index permutation, such that there is a natural association between the sign of m and the vortex orientation.

To produce a 3D visualization, one fixes the value of λ in Eq. (7) to be the dimension upon which slices are taken. The remaining three dimensions comprise the slice, such that the plaquettes now may be written as

$$P_{ij}(\mathbf{x}) = \exp\left(\frac{2\pi i}{3}\epsilon_{ijk}m_{k\lambda}(\bar{\mathbf{x}})\right), \qquad (8)$$

where the Latin indices enumerate the three dimensions orthogonal to the fixed λ. Using this definition, a vortex is rendered as a jet of length a, pointing in the $m_{k\lambda}(\bar{\mathbf{x}})\hat{k}$ direction that pierces the $P_{ij}(x)$ plaquette. For example, if we choose $\lambda = 4$, a $m = +1$ vortex identified by $P_{xy}(n)$ would be rendered in the $+\hat{z}$ direction. This rendering convention is illustrated in Fig. 8.

A notable feature of $SU(3)$ center vortices is the presence of vortex branching. Due to the periodicity of the nontrivial center phases in $\mathbb{Z}_3$, one unit of positive center charge is equivalent to two units of negative center
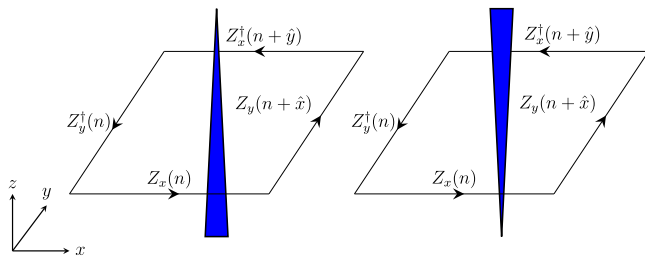
FIG. 8.   The spacial vortex plotting convention with $\lambda = 4$. An $m = +1$ vortex (*left*) identified by the plaquette $P_{xy}(n)$ is rendered in the $\hat{z}$ direction. An $m = -1$ vortex (*right*) identified by the same plaquette is rendered in the $-\hat{z}$ direction.

charge. Hence, within a 3D slice a vortex line carrying $m = +1$ charge may branch into two $m = -1$ vortex lines. Note that this process is indistinguishable from three $m = +1$ vortex lines converging to the vacuum, as illustrated in Fig. 11. Recall that our visualizations illustrate the directed flow of $m = +1$ charge. This is why these branching points are also sometimes referred to as vortex monopoles and antimonopoles in the literature [26]. This ambiguity in charge assignment has important ramifications for center vortex topology, as discussed in Ref. [9].

For the purposes of this work, we will refer to intersections of three or five vortices as branching points. Intersections of four vortices occur at the intersection of vortex lines and do not constitute vortex branching. They are thus excluded from the branching-point analysis. Finally, intersections of six vortices could arise from either vortex branching or the intersection of three vortex lines. As these situations are indistinguishable, for this work we will consider these points to be branching points. However, it must be noted that the occurrence of six-way branching points is so infrequent that this choice has an insignificant impact on branching-point statistics.

A straightforward nomenclature for referring to branching points [26] is to define the branching genus $n_{\text{cube}}(x|\hat{\mu})$. Here, $\hat{\mu}$ denotes the direction along which the lattice has been sliced and hence identifies the remaining three coordinates, $\hat{i}, \hat{j}, \hat{k}$, that describe the location within the 3D slice. Within the selected slice, we define $\mathbf{x}'$ to denote the dual lattice site, $\mathbf{x}' = \mathbf{x} + \frac{a}{2}(\hat{i} + \hat{j} + \hat{k})$. $n_{\text{cube}}(x|\hat{\mu})$ then counts the number of vortices piercing the elementary cube around $\mathbf{x}'$. Thus, we have the following interpretation for the possible values of $n_{\text{cube}}(x|\hat{\mu})$:

$$n_{\text{cube}}(x|\hat{\mu}) = \begin{cases} 0 & \text{No vortex} \\ 2 & \text{regular vortex line} \\ 3, 5, 6 & \text{branching point} \\ 4 & \text{touching point} \end{cases} \quad (9)$$

The normalized distribution of values of n_{cube} across the three ensembles is shown in Fig. 9. We observe that the
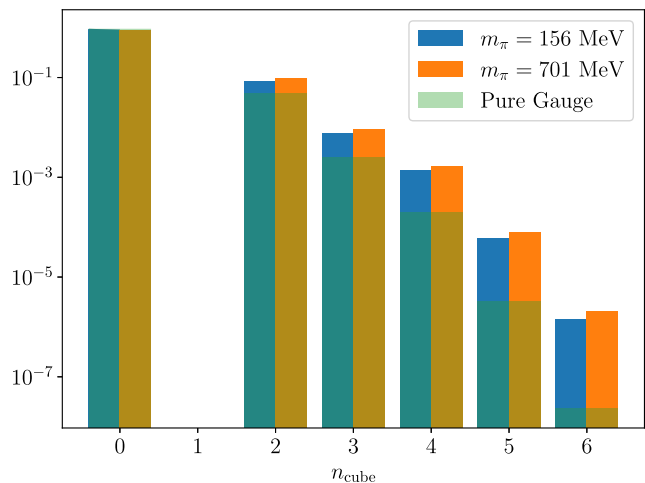
FIG. 9.   The distribution of branching-point genera as defined in Eq. (9).

distribution of the higher genus values decreases monotonically for all ensembles. The dynamical ensembles feature a greater probability of high-multiplicity branching points. This predicts a greater vortex density for these ensembles relative to the pure gauge case, as will be discussed in the next section.

V. CLUSTER IDENTIFICATION

It is well-known that for $SU(2)$ gauge fields in the confining phase, percolation of center vortices can be used as an order parameter for the transition from the confined phase to the deconfined phase [6,8]. At a glance, the visualizations constructed in Ref. [32] support this assessment, with a single large connected vortex cluster clearly visible in each visualization and only a handful of separate smaller secondary clusters present. Studying the confinement phase transition at the critical temperature will be the subject of future work. However, it is of interest to build the necessary tools to perform such a study. This requires us to quantitatively understand the degree to which a vortex ensemble is dominated by a primary percolating cluster, as opposed to a collection of smaller secondary clusters. To do this, it is necessary to develop an algorithm that can trace these vortex lines and identify disconnected clusters.

Such an analysis is quite straightforward in $SU(2)$, as $SU(2)$ vortices do not permit branching points. This simplifies the algorithm, as each vortex cluster consists of a single line that may be followed until it arrives back at its starting location. In $SU(3)$, vortex branching demands that the algorithm track multiple branching paths, and only terminates when there are no continuations for every path. We describe such an algorithm here.

The starting point for the algorithm is to have all vortices in a 3D slice stored along with their associated tip and base coordinates. With this setup, the algorithm proceeds as follows:
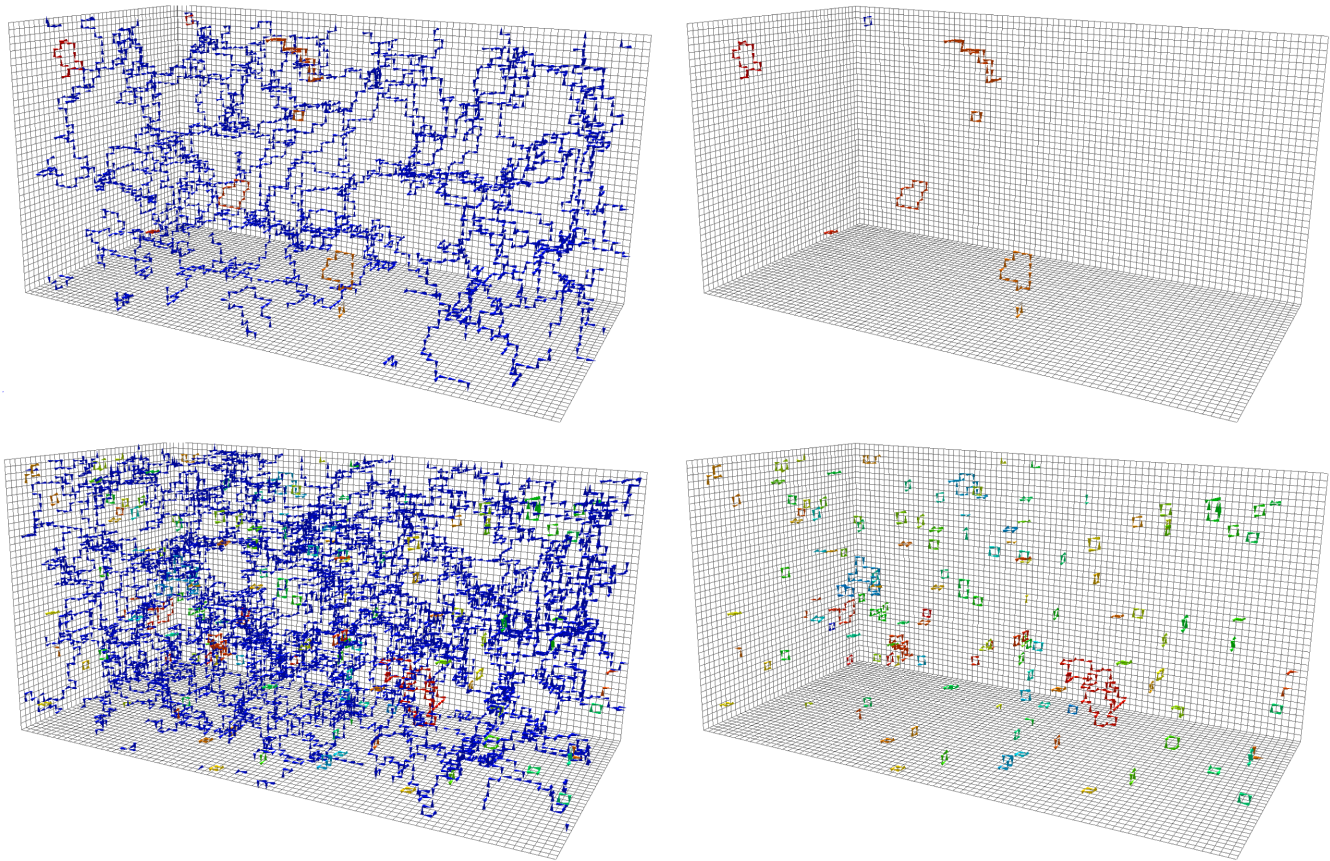
FIG. 10. (Top left) The center vortex structure of a pure-gauge configuration. (Top right) The pure-gauge vortex vacuum as shown in the top left panel with the primary percolating vortex cluster removed. (Bottom left) The center-vortex structure of a $(2 + 1)$-flavor dynamical-fermion configuration from the $m_\pi = 156$ MeV ensemble. (Bottom Right) The dynamical vortex structure in the bottom-left panel with the primary percolating vortex cluster removed. Note the increased abundance of elementary vortex paths and the prevalence of branching points. In each panel, separate vortex clusters are rendered with different colors. These 3D models are generated with AVS scientific visualization software [39]. (*Interactive* in the supplemental material [33].).

(1) Choose an arbitrary vortex to start at. Mark it as visited and record it as belonging to an incomplete line segment.

(2) Considering the last vortex in each incomplete line segment, produce a list of all unvisited vortices touching this vortex (both base and tip, accounting for periodicity). Then mark them all as visited

(3) Append one of the found vortices to the current segment. For all others, begin a new segment.

(4) If there are incomplete segments, repeat from step 2 for each incomplete segment.

(5) Once there are no unvisited touching vortices, mark the segment as complete.

(6) If all segments are complete, the cluster is complete. Record all vortices in all segments as belonging to this cluster. Return to step 1, selecting an unvisited vortex.

(7) If there are no unvisited vortices, all clusters have been identified and the algorithm is complete.

This algorithm can then be applied to each 3D slice to isolate all independent vortex clusters.

Employing this algorithm and our visualization conventions defined in Sec. IV, the pure-gauge vortex vacuum on a single slice appears as in top-left panel of Fig. 10. The interactive version of this visualization may be found in Fig. S-1 Supplemental Material (SM) [33]. As our investigation takes place at zero temperature on a large volume lattice, the choice of slice direction does not impact most intrinsic measurements, and as such we choose to present plots obtained from slicing in the $\hat{x}$ direction. The only notable exception is the size of the percolating cluster as it fills the 3D volume and is therefore smaller for $\hat{t}$ slices. The choice of $\hat{x}$ will be assumed for the remainder of this work unless stated otherwise. Numerical values presented in tables will be averaged across all slice dimensions, where applicable.

We observe that indeed the vacuum is dominated by a single primary percolating cluster, with an assortment of small secondary clusters also present. Branching points are readily observed within the visualization, as can be seen in Fig. 11 and in the interactive view 'Branching Points' Fig. S-1 in SM [33].
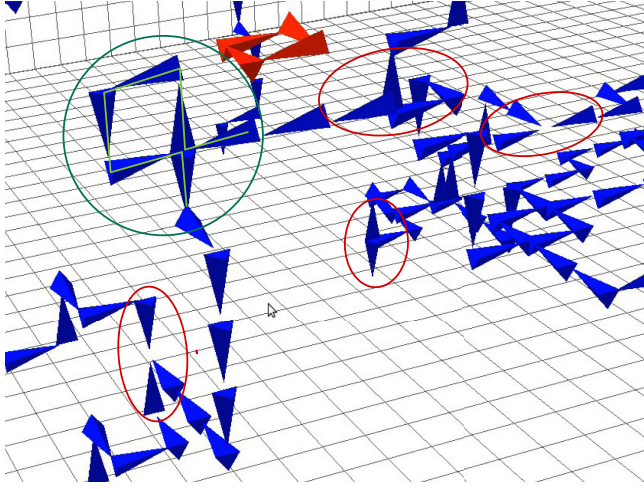
FIG. 11. A collection of branching points (red ovals), a touching point (green circle) and a secondary loop (red jets) as they appear in our visualizations. Each jet illustrates the flow of $m = +1$ center charge.

TABLE II. The average number of vortices associated with the total per 3D slice (N_{slice}), the primary cluster (N_{primary}), and a secondary cluster ($N_{\text{secondary}}$), as calculated on the three ensembles. Separate averages are listed for the slicing dimension $\hat{\mu}$ being temporal or spatial.

	$\hat{t}$	$\hat{x}, \hat{y}, \hat{z}$
Pure gauge		
N_{slice}	1673(3)	3347(6)
N_{primary}	1638(3)	3277(6)
$N_{\text{secondary}}$	7.32(5)	7.40(3)
701 MeV		
N_{slice}	3651(4)	7302(8)
N_{primary}	3366(4)	6731(8)
$N_{\text{secondary}}$	5.047(5)	5.057(3)
156 MeV		
N_{slice}	3227(4)	6452(8)
N_{primary}	2964(4)	5926(9)
$N_{\text{secondary}}$	5.011(5)	5.018(3)

The transition to full QCD leads to a marked shift in the behavior of the center vortices, as can be seen from the vortex vacuum of the lightest-pion mass ensemble shown in the bottom-left panel of Fig. 10. The interactive version of this visualization may be found in Fig. S-2 in SM [33]. The total number of vortices has increased significantly.

The dominance of a single vortex cluster is even more pronounced once it is removed, as shown in the right-hand panels of Fig. 10 for the pure-gauge (top) and dynamical-fermion (bottom) slices. Almost all the vortex matter is associated with the percolating cluster. However, if we focus on the dynamical-fermion secondary clusters in the bottom-right panel of Fig. 10, we see that the number of secondary clusters has increased substantially when compared to the pure gauge ensemble. Moreover, an increase in the complexity of the secondary structures through branching-point clusters is also evident.

These secondary clusters may also be explored in the interactive models given in Figs. S-3 and S-4 in SM [33] for the pure-gauge and dynamical-fermion cases. There several features are highlighted in the "Views" menu and these views are also available in the full vortex illustrations of Figs. S-1 and S-2 in SM [33].

To gauge the relative sizes of the primary and secondary clusters, we calculate the average total number of vortices per slice, N_{slice}, the average number of vortices associated with the primary cluster, N_{primary}, and the average number of vortices associated with a secondary cluster, $N_{\text{secondary}}$. N_{slice}, N_{primary}, and $N_{\text{secondary}}$ for all three ensembles are presented in Table II. Note that the spatial values are obtained by averaging across the three spatial dimensions acting as the slice dimension. When $\hat{t}$ is selected for slicing the four-dimensional volume, the spatial volume is half that when a spatial direction is selected. As such, the

percolating cluster values in the $\hat{t}$ column are expected to be half those in the spatial slicing column.

Interestingly, we observe that $N_{\text{secondary}}$ decreases in the presence of dynamical fermions, indicating that the secondary clusters are smaller on average. This is due to a proliferation of elementary plaquette vortex paths in dynamical fermion QCD, as illustrated in the bottom-right panel of Fig. 10.

We also see that N_{slice} and N_{primary} from the heavier quark-mass ensemble are larger than the values calculated on the light ensemble. This is likely a result of the fact that the heavier pion mass configurations have a slightly larger physical volume. We can determine if this is the case by considering the vortex density, ρ_{vortex}.

The vortex density is calculated by considering the proportion of plaquettes that are pierced by a vortex, P_{vortex}. This is best calculated by first defining an indicator function,

$$v_{\mu\nu}(x) = \begin{cases} 1, & P_{\mu\nu}(x) = \exp\left(\frac{\pm 2\pi i}{3}\right)I \\ 0, & P_{\mu\nu}(x) = I. \end{cases} \tag{10}$$

We then calculate the proportion of pierced plaquettes as

$$P_{\text{vortex}} = \frac{1}{6V}\sum_{\substack{\mu,\nu \\ \mu<\nu}}\sum_{x} v_{\mu\nu}(x), \tag{11}$$

where the value 6 counts the number of plaquettes associated with site x in four dimensions and $V = N_x N_y N_z N_t$ counts the number of sites in the sum over x. The physical density is then given by

TABLE III. The vortex density as calculated on the three ensembles. The proportion of pierced plaquettes, P_{vortex}, the physical vortex density, ρ_{vortex}, the proportion of branching points, P_{branch} and the physical branching-point density, ρ_{branch} are presented.

Ensemble	P_{vortex}	ρ_{vortex} (fm^{-2})	P_{branch}	ρ_{branch} (fm^{-3})
Pure gauge	0.01702(3)	1.702(3)	0.00249(1)	2.49(1)
701 MeV	0.03714(4)	3.556(4)	0.00897(1)	8.41(1)
156 MeV	0.03282(4)	3.770(5)	0.00753(1)	9.27(2)

$$\rho_{\text{vortex}} = \frac{P_{\text{vortex}}}{a^2}. \qquad (12)$$

In the case where the vortex distribution is isotropic, the density derived in four dimensions is equal to the mean of the three-dimensional density when averaged over slices (such as in Fig. 10). We can decompose the lattice coordinates into a $1+3$-dimensional notation, $x = (w, \mathbf{x}|\hat{\mu})$, with w corresponding to the index in the slicing dimension $\hat{\mu}$ and $\mathbf{x}$ specifying the location within the corresponding hyperplane. Then the vortex density for slice w along the dimension $\hat{\mu}$ is

$$P_3(w, \hat{\mu}) = \frac{1}{3V_3(\hat{\mu})} \sum_{\substack{i,j \\ i<j,\neq\mu}} \sum_{\mathbf{x}} v_{ij}(w, \mathbf{x}|\hat{\mu}), \qquad (13)$$

where $v_{ij}(w, \mathbf{x}|\hat{\mu})$ is the restriction of the indicator function in Eq. (10) to the relevant slice, $V_3(\hat{\mu})$ is the corresponding 3-volume (e.g. $V_3(\hat{x}) = N_y N_z N_t$), and the division by 3 averages the number of plaquettes associated with each site in three dimensions.

Upon averaging over all w slices in a given dimension and then averaging over the four slice directions, one finds the following for the mean density

$$\bar{P}_3 = \frac{1}{3V} \frac{1}{4} \sum_{\mu} \sum_{\substack{i,j \\ i<j,\neq\mu}} \sum_{w,\mathbf{x}} v_{ij}(w, \mathbf{x}|\hat{\mu}). \qquad (14)$$

Noting that each plaquette has been counted twice in the sum over i, j and μ, one recovers P_{vortex} of Eq. (11). Of course, in both cases, the physical density is governed by the area of the plaquette as in Eq. (12).

The vortex densities from the three ensembles are shown in Table III. We see that the ρ_{vortex} is indeed larger on the ensemble with the lightest pion mass, indicating a consistent trend of increasing vortex density as the physical pion mass is approached from above.

Another quantity of interest is the branching-point density. This is obtained by considering the fraction of elementary cubes within each 3D slice that contain a branching point, P_{branch}. Again, this is best calculated by first considering the indicator function
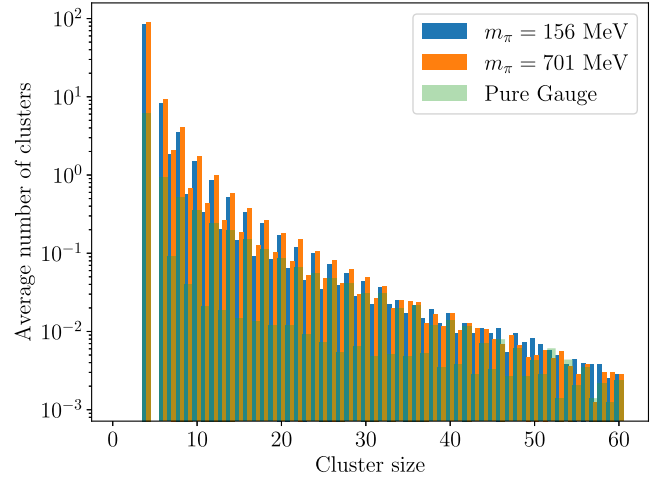
FIG. 12. Average number of secondary clusters of a given size per slice, up to a cutoff size of 60.

$$b(x|\hat{\mu}) = \begin{cases} 1, & n_{\text{cube}}(x|\hat{\mu}) = 3, 5, 6 \\ 0, & \text{otherwise.} \end{cases} \qquad (15)$$

The branching-point proportion is then given by

$$P_{\text{branch}} = \frac{1}{4V} \sum_{\mu} \sum_{x} b(x|\hat{\mu}), \qquad (16)$$

where μ sums over all four dimensions. As this density is defined as an average over 3D cubes, the associated physical density is

$$\rho_{\text{branch}} = \frac{P_{\text{branch}}}{a^3}. \qquad (17)$$

The branching-point density is shown in Table III. Here we observe that the branching-point density follows the same trend as the vortex density, namely that it increases with decreasing dynamical quark mass.

To quantify the change in the behavior of $N_{\text{secondary}}$ recorded in Table II we count the number of clusters of a given size and average across slices and the ensemble. These results are shown in Fig. 12. There are a number of interesting features present here. Firstly, it is clear that it is not possible to have clusters containing less than four vortices, and that it is also not possible to have five vortices in a cluster. There is an interesting trend that the number of clusters containing an even number of vortices is higher than the number containing an odd number of vortices, especially at small cluster sizes. This results in the alternating comb pattern present in Fig. 12. This is a result of the fact that a branching point is necessary for a cluster to contain an odd number of vortices. Hence, this alternating pattern speaks to the presence of a 'cost' associated with a branching point, resulting in clusters containing branching points being less probable than those without. This effect is
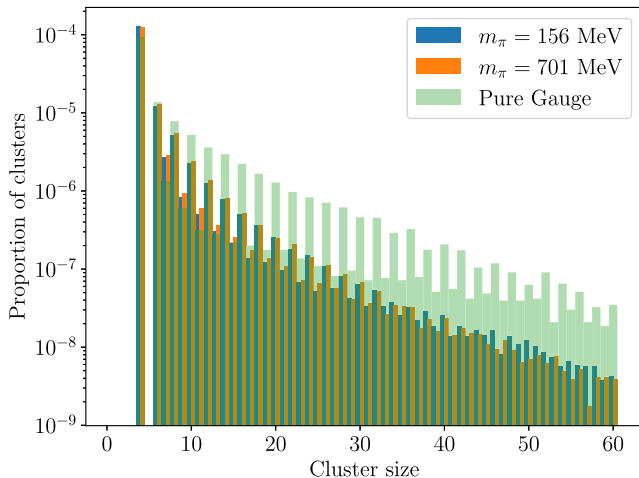
FIG. 13. Proportion of secondary clusters of a given size per slice, normalized by the total number of clusters, both primary and secondary, in their respective ensemble.

FIG. 14. Histogram of both primary and secondary cluster extents relative to $L_{\max}$ for all three ensembles, as described in the text. It is clear that the vortex vacuum at zero temperature is dominated by a single percolating cluster, as can be seen by the dominance of the bin containing the clusters of maximal extent. Bin widths are 0.1 and are centered at the tick marks of the x-axis.

mitigated as the cluster size increases and the number of vortex arrangements leading to that cluster size increases.

Comparing the different ensembles, we find that the number of clusters at each size on the dynamical ensembles exceed almost all of the pure gauge clusters. However, if we normalize the histogram by the total number of clusters found in the ensemble, as shown in Fig. 13, we find that the pure gauge ensembles have a comparable or greater proportion of larger secondary clusters present, perhaps due to the low vortex density. We observe that the dynamical ensembles still retain a larger proportion of the smallest secondary clusters.

We can measure the size of a cluster by defining the cluster extent as the largest pairwise distance between vortices belonging to the same cluster, as done in Ref. [8]. The cluster extents are binned, and the content of each bin represents the average number of vortices in the associated cluster, relative to the total number of vortices in the ensemble. The cluster extents are normalized by the greatest distance on a $N_y \times N_z \times N_t$ slice of a periodic lattice,

$$L_{\max} = \sqrt{(N_y/2)^2 + (N_z/2)^2 + (N_t/2)^2}. \quad (18)$$

The results of this analysis for our three ensembles is shown in Fig. 14.

The cluster extents shown in Fig. 14 clearly demonstrate that at zero temperature the $SU(3)$ vortex vacuum is dominated by a single percolating vortex cluster, with only a minority of vortices comprising smaller secondary loops. It is expected that this situation will change as the temperature exceeds the critical temperature, as has been observed in $SU(2)$ gauge theory [8]. We also observe that the pure gauge secondary clusters tend to be larger than their dynamical counterparts.

We find that the vortex and branching-point density significantly increases upon the introduction of dynamical fermions. However, relative to the total number of vortices present, the pure gauge sector contains a greater proportion of larger secondary clusters than the dynamical case. Aside from the primary vortex cluster, the dynamical vortex vacuum is dominated by an excess of very small secondary clusters. The visualizations reveal significant branching-point complexity in the large secondary clusters of the dynamical-fermion vortex vacuum. Several features are highlighted in the "Views" menu of the interactive figures provided in the supplemental material [33].

VI. BRANCHING-POINT GRAPHS

The cluster analysis presented in Sec. V enables us to gain insight into the size of the primary and secondary vortex clusters. It is also of interest to study the relationship between branching points, as these structures are absent in $SU(2)$ where much of the analysis of vortex structure has previously been performed. Furthermore, it is helpful to abstract the vortex clusters such that we need not be concerned with their precise 3D coordinates. To that end, we seek to represent vortex clusters as a directed graph, with branching points acting as vertices and the edges being given by vortex lines, with each edge weighted by the number of vortices in the line.

The algorithm to perform this graph construction starts with an identified vortex cluster as defined in Sec. V. First, for each vortex we evaluate whether it touches a point with $n_{\mathrm{cube}}(x|\hat{\mu}) \geq 3$ at its tip, base, both or neither. Each branching or touching point should also have a unique ID. The algorithm proceeds as follows:
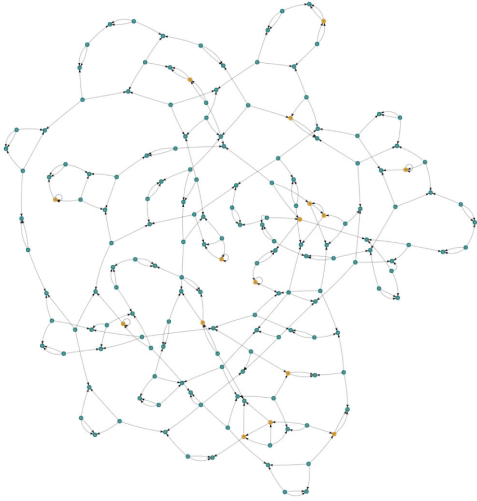
FIG. 15. The pure-gauge primary vortex cluster from the slice shown in the top-left panel of Fig. 10 rendered as a graph. Branching/touching points are the vertices and connecting vortex lines are the edges. Blue vertices indicate three-way branching points and orange vertices indicate four-way touching points. Visualizations were generated with the Pyvis visualization package [40].
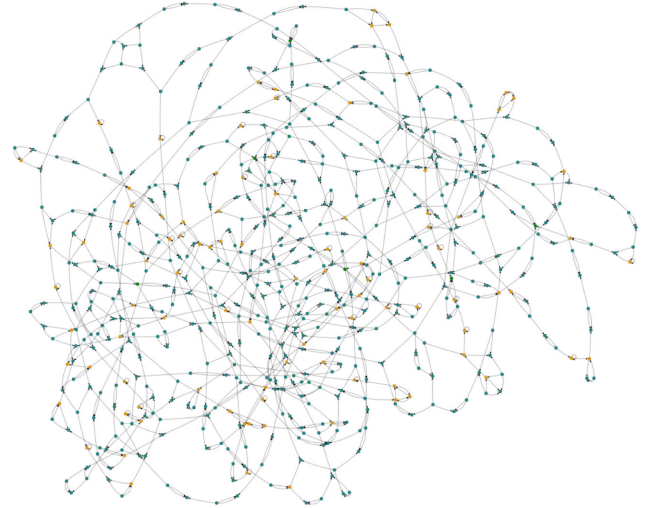
(1) Find an untraversed vortex with a branching/touching point at its base. If no untraversed vortex can be found, then we are done. Otherwise, set the found vortex to be the current vortex and mark it as traversed. Set the current interbranching point distance to 1 and record the ID of the branching/touching point at the base.

(2) Check if the current vortex has a branching/touching point at its tip. If it does, create an edge between the saved branching/touching point ID and the ID of the branching/touching point at the tip with weight equal to the current interbranching point distance. Return to step 1.

(3) Otherwise, find the vortex with its base touching the tip of the current vortex and mark it as traversed. Set the new vortex to be the current vortex and add 1 to the interbranching point distance. Return to step 2.

The resulting graph encodes the separations between all branching and touching points within a cluster without reference to the specific cluster geometry.

Applying this algorithm to the primary clusters shown in Fig. 10 for pure gauge and dynamical vacuum fields, we produce the graphs shown in Figs. 15 and 16 respectively. These visualizations clearly demonstrate the significant increase in vortices and branching points present on the dynamical configurations.

Utilising this new construction, we wish to determine a measure of the separation between connected branching points. A pair of branching points may be connected via multiple vortex lines, and these lines may also pass through touching points that we wish to exclude from the

calculation. The presence of these touching points makes it impossible to devise a unique distance between two branching points, as this distance will depend on the manner in which the touching point is traversed, as shown in Fig. 17. Instead, we devise an algorithm for calculating the interbranching point distance that enables a random selection of directions with which to traverse these touching point vertices. The algorithm proceeds as follows:

(1) Randomly choose a branching-point vertex with untraversed outgoing edges. Record the vertex as the first in a path. Set the current path length to 0.

FIG. 16. The $m_\pi = 156$ MeV primary vortex cluster from the slice shown in the bottom-left panel of Fig. 10 rendered as a graph. Plotting conventions are as described in Fig. 15.
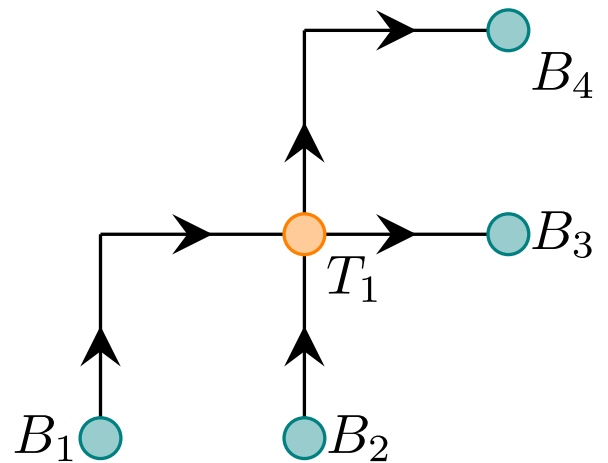
FIG. 17. An example of how the touching point T_1 introduces ambiguity into the distance between branching points, B_i. B_1 can connect to either B_3 or B_4, with B_2 then connecting to B_4 or B_3, respectively. This would result in either distances of 4, 2 or 3, 3 being recorded by our algorithm, depending on the order of traversal.

If there is no vertex with an untraversed outgoing edge then we are done.

(2) Randomly choose an untraversed outgoing edge to follow to a new vertex. Mark the chosen edge as traversed, add the new vertex to the current path and add its length to the path length.

(3) If this edge arrives at a branching point, store the path and the current path length and return to step 1.

(4) If the edge arrives at a touching point, repeat from step 2 with the new vertex as the starting vertex.

The end result of this algorithm is a list of paths between branching points that permit the ability to pass through touching points. However, not all edges will be traversed by this method, as the presence of touching points allows for cycles to emerge from these paths. Fortunately, due to conservation of vortex flux, any cycle emerging from a given path will return to that same path. Hence to rectify the algorithm, we simply need to traverse all cycles on a given path and add their length to the existing length. This is done by performing a modified depth-first search on each vertex to traverse any cycles that were omitted from the above method. Pseudocode for this search on a single vertex is as follows:

Algorithm 1.

```
function dfs (this_vertex, path):
  for edge in this_vertex. edges:
    if (edge is not traversed
        and edge is outgoing):
      path.length+= edge.length
      edge.traversed = True
      next_vertex = edge.end
      if next_vertex is not this_vertex:
        dfs (next_vertex, path)
```

The path lengths now accurately represent the distance between branching points. This concludes our determination of the branching-point separations. Note that because of the inherent ambiguities in the branching-point graphs, the solution is not unique. We determine whether the impact of this randomness is significant in the ensemble average choosing a single calculation of the distances as a reference, then repeating the distance calculation nine further times with different random seeds.

We then use the Kolmogorov-Smirnov test [41] to determine the equality of the different distributions. We find that the test statistic for all ensembles is of order 10^{-5}, with corresponding p-values consistent with 1. Thus we are satisfied that the variance in this distance measure is negligible in the ensemble average, and we are therefore justified in considering it a useful measure of branching-point separation.

The average separation, d, for each ensemble is presented in Table IV. The physical separation $\Delta = ad$ is also determined. Here we see that there is a consistent trend of decreasing average separation with decreasing pion mass. This coincides with our determination of the branching-point and vortex densities, as a higher density suggests a smaller separation between points.

We also present the average number of edges in the graphs, n_{edges}, and the average number of edges per node, $n_{\text{edges}}/n_{\text{nodes}}$ in Table IV as measures of the complexity and structure of the graphs. We observe that, as expected, the number of edges substantially increases upon the introduction of dynamical fermions. The number of edges per node is close to 1.5 for all ensembles, as the majority of edges emerge from a three-way branching point and terminate at another three-way branching point. However, the number of edges per node is larger on the dynamical ensembles, likely due to the increase in vortex density resulting in a higher number of vortex intersections.

The distribution of branching-point separations is shown in Fig. 18. The results are normalized by the total number of vortex paths considered, such that the histogram has unit area. Apart from an enhancement of the smallest branching-point separations, the distances are exponentially distributed. This distribution is consistent with a constant branching probability, i.e., the probability of branching at the next link of a vortex chain is independent of the length of the vortex chain.

This supports a previous conjecture for the interpretation of vortex branching [26,31]: that a vortex can be considered to have some fixed rate of branching as it propagates through spacetime. This interpretation allows for vortex branching on the lattice to be considered as a binomial random variable X with some probability of branching, q. Thus, the probability of branching after k lattice plaquettes is given by the geometric distribution

TABLE IV. The average distance between branching points, d, the same distance in physical units, Δ, the average number of edges per graph, n_{edges}, and the average number of edges per node, $n_{\text{edges}}/n_{\text{nodes}}$.

Ensemble	d	Δ (fm)	n_{edges}	ρ_{edges} (fm^{-3})	$n_{\text{edges}}/n_{\text{nodes}}$
Pure gauge	13.55(2)	1.355(2)	238(1)	4.14(1)	1.53849(8)
701 MeV	7.691(4)	0.7860(4)	970(1)	15.84(2)	1.58667(6)
156 MeV	8.082(5)	0.7541(5)	807(1)	17.32(3)	1.58332(7)
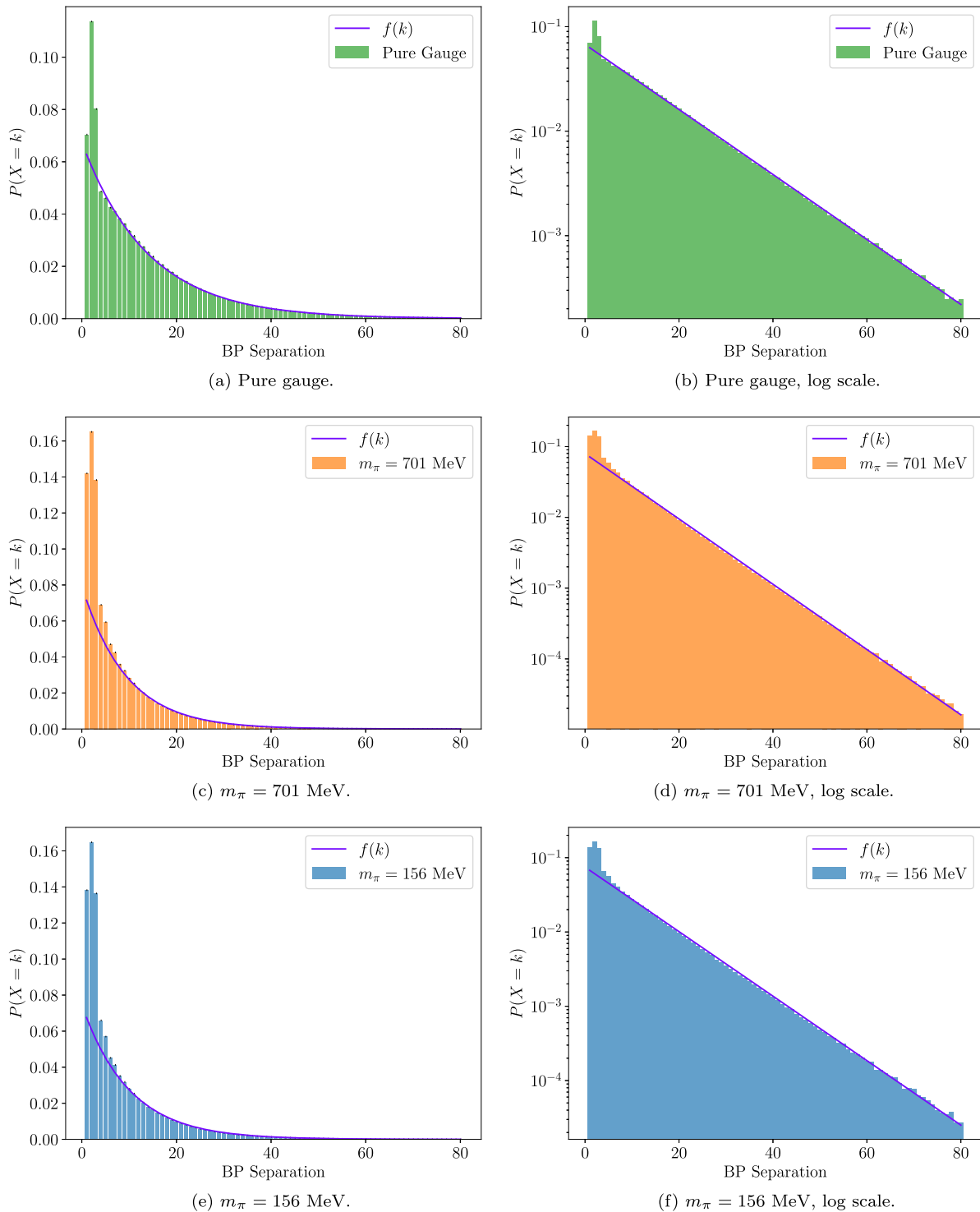
FIG. 18.   Normalized branching-point (BP) separations from all ensembles, along with the corresponding fit to $f(k)$ given in Eq. (20).

$$P_k = q(1 - q)^{k-1}. \tag{19}$$

Typically, one estimates the rate of a binomial random variable by evaluating $q = 1/\bar{X}$, where $\bar{X} = \sum_k k P_k$. However, due to the deviations from linearity found at

small separations in the log-distributions shown in Fig. 18, this measure fails to capture the true rate of branching. To account for this, we instead fit a linear function,

$$f(k) = \alpha - \beta k, \tag{20}$$

TABLE V.   The naive and fitted branching rates, q_{naive} and q, and their physical counterparts λ_{naive} and λ obtained through the methods described in the text. The fit parameter β is also presented. Only q and λ are associated with a constant branching probability.

Ensemble	q_{naive}	λ_{naive} (fm^{-1})	q	λ (fm^{-1})	β
Pure gauge	0.05010(6)	0.5010(6)	0.0690(2)	0.690(2)	0.0715(2)
701 MeV	0.08526(5)	0.8342(5)	0.1005(3)	0.984(3)	0.1059(3)
156 MeV	0.08062(6)	0.8641(7)	0.0952(2)	1.020(3)	0.1000(3)

to the log of the distribution of branching-point separations for $k > 3$. The result of this fit for each ensemble is plotted in Fig. 18.

Of course, for a normalized distribution, α is constrained by β. However, the significant nonexponential behavior for $k \leq 3$ spoils the exponential normalization constraint. Thus α is introduced to accommodate for this, and we refer to β describing the k dependence to determine the branching probability q.

The parameters of this fit are related to the log of the binomial rate

$$\log(P_k) = \log(q) - \log(1-q) + \log(1-q)k = \alpha - \beta k. \tag{21}$$

Equating the coefficients of the terms linear in k, we resolve the branching rate

$$q = 1 - e^{-\beta}. \tag{22}$$

Note, for small β, $q = \beta$. This rate can be converted to a physical quantity by then considering the rate per unit length, $\lambda = q/a$. All fitted parameters are calculated on 200 bootstrap ensembles, with errors determined via the bootstrap variance.

The rate described above can then be compared to the naive rate, q_{naive}, calculated by considering the number of cubes containing branching points divided by the number of cubes pierced by two or more vortices. Defining

$$c(x|\hat{\mu}) = \begin{cases} 1, & n_{\text{cube}}(x|\hat{\mu}) \neq 0 \\ 0, & \text{otherwise,} \end{cases} \tag{23}$$

and recalling the branching-point indicator defined in Eq. (15), we define the naive rate to be

$$q_{\text{naive}} = \frac{\sum_\mu \sum_x b(x|\hat{\mu})}{\sum_\mu \sum_x c(x|\hat{\mu})}. \tag{24}$$

The associated physical quantity is the rate per unit length, $\lambda_{\text{naive}} = q_{\text{naive}}/a$. The calculated rate parameters from both methods are shown in Table V. We observe that with both measures the physical branching rate increases as the physical pion mass is approached. We emphasize, only q contains the detailed information on the path geometry.

The difference between the fitted and naive rates is an interesting finding. The naive rate will include the short-range nonexponential behavior, inconsistent with a constant branching rate. At larger separations, vortex branching follows a constant rate. However, there are clearly short-range effects that result in clustering of branching points, which in turn necessitates the more sophisticated approach detailed above for q. These clustering effects appear to be amplified upon introduction of dynamical fermions. Whether this clustering radius is a physical effect or the result of finite lattice-spacing effects is an interesting avenue for future study.

It should be noted that whilst the distributions shown in Fig. 18 take into account all primary and secondary clusters, the results are minimally affected if the secondary clusters are removed due to the vast majority of branching points belonging to the primary cluster.

An interesting correlation we observe is that the ratio between the pure gauge and dynamical branching rates is similar to the corresponding ratio of the vortex-only string tensions calculated in Ref. [27]. The vortex density is naturally correlated with the branching rate. In SU(2) at least, it has been shown through simple combinatoric arguments that the Wilson-loop area law and hence the string tension can be related to the density of percolating random vortices [42]. It seems reasonable to infer then that the correlation we observe between the branching-rate and string-tension ratios is not simply a coincidence but a reflection of the differing structure of the vortex fields in the pure-gauge and dynamical sectors.

VII. CONCLUSION

In this work we have explored of the impact of dynamical fermions on the center-vortex structure of the vacuum ground-state fields.

Examining the bulk properties of the original gauge fields, we find that dynamical fermions lead to greater off-diagonal strength in the lattice gauge links. The presence of dynamical fermions gives rise to an increased abundance of center vortices and branching points, as reflected by the increasing vortex and branching-point densities as the physical pion mass is approached.

We construct cluster identification algorithms to identify independent vortex clusters and use this identification to construct visualizations of the vortex vacuum. These reveal that the vacuum is dominated by a single percolating

cluster. Our results show that dynamical fermions lead to an abundance of smaller clusters as compared to their pure-gauge counterparts.

We employ a novel method of reducing vortex clusters to directed graphs, with vertices defined by branching points and edges connecting them weighted by the number of vortex links. Using this construction, we render the graphs to illustrate the radical change in the number of vortices and branching points after the introduction of dynamical fermions. We define a measure of branching-point separation, and observe that the distribution of separations follows an approximate geometric distribution. We estimate the rate of this distribution and find that there is a tendency for branching points to cluster at small separations.

Understanding the role of dynamical quarks in the QCD vacuum continues to be an interesting area of study. The effect of matter fields on the vacuum phase structure has been explored elsewhere within the gauge-Higgs model [43–46]. The extension of these ideas to QCD may shed further light on the nature of confinement. In particular, investigations that further our understanding of string breaking in terms of QCD vacuum structure is desirable.

The findings of this paper illustrate the substantial impact dynamical fermions have on the geometry and structure of the center vortex vacuum. These results add to the growing body of evidence [27,28] for the effect of dynamical fermions on center vortices as compared to the well-established pure-gauge sector. The relationship between the vortex geometry analyzed here and the shift in observable behavior is still a subject of great interest. Future work is also intended to explore how this geometry changes in the finite-temperature regime.

ACKNOWLEDGMENTS

[1] G. 't Hooft, On the phase transition towards permanent quark confinement, Nucl. Phys. **B138**, 1 (1978).

[2] G. 't Hooft, A property of electric and magnetic flux in non-Abelian gauge theories, Nucl. Phys. **B153**, 141 (1979).

[3] L. Del Debbio, M. Faber, J. Greensite, and S. Olejnik, Center dominance and Z(2) vortices in SU(2) lattice gauge theory, Phys. Rev. D **55**, 2298 (1997).

[4] M. Faber, J. Greensite, and S. Olejnik, Casimir scaling from center vortices: Towards an understanding of the adjoint string tension, Phys. Rev. D **57**, 2603 (1998).

[5] L. Del Debbio, M. Faber, J. Giedt, J. Greensite, and S. Olejnik, Detection of center vortices in the lattice Yang-Mills vacuum, Phys. Rev. D **58**, 094501 (1998).

[6] R. Bertle, M. Faber, J. Greensite, and S. Olejnik, The structure of projected center vortices in lattice gauge theory, J. High Energy Phys. 03 (1999) 019.

[7] M. Faber, J. Greensite, S. Olejnik, and D. Yamada, The vortex finding property of maximal center (and other) gauges, J. High Energy Phys. 12 (1999) 012.

[8] M. Engelhardt, K. Langfeld, H. Reinhardt, and O. Tennert, Deconfinement in SU(2) Yang-Mills theory as a center vortex percolation transition, Phys. Rev. D **61**, 054504 (2000).

[9] M. Engelhardt and H. Reinhardt, Center projection vortices in continuum Yang-Mills theory, Nucl. Phys. **B567**, 249 (2000).

[10] M. Engelhardt, Center vortex model for the infrared sector of Yang-Mills theory: Topological susceptibility, Nucl. Phys. **B585**, 614 (2000).

[11] R. Bertle, M. Faber, J. Greensite, and S. Olejnik, P vortices, gauge copies, and lattice size, J. High Energy Phys. 10 (2000) 007.

[12] K. Langfeld, H. Reinhardt, and J. Gattnar, Gluon propagators and quark confinement, Nucl. Phys. **B621**, 131 (2002).

[13] J. Greensite, The confinement problem in lattice gauge theory, Prog. Part. Nucl. Phys. **51**, 1 (2003).

[14] F. Bruckmann and M. Engelhardt, Writhe of center vortices and topological charge: An explicit example, Phys. Rev. D **68**, 105011 (2003).

[15] M. Engelhardt, M. Quandt, and H. Reinhardt, Center vortex model for the infrared sector of SU(3) Yang-Mills theory: Confinement and deconfinement, Nucl. Phys. **B685**, 227 (2004).

[16] P. Y. Boyko, V. G. Bornyakov, E. M. Ilgenfritz, A. V. Kovalenko, B. V. Martemyanov, M. Muller-Preussker, M. I. Polikarpov, and A. I. Veselov, Once more on the interrelation between Abelian monopoles and P-vortices in SU(2) LGT, Nucl. Phys. **B756**, 71 (2006).

[17] E.-M. Ilgenfritz, K. Koller, Y. Koma, G. Schierholz, T. Streuer, V. Weinberg, and M. Quandt, Localization of overlap modes and topological charge, vortices and monopoles in SU(3) LGT, Proc. Sci., LATTICE2007 (**2007**) 311 [arXiv:0710.2607].

[18] V. G. Bornyakov, E. M. Ilgenfritz, B. V. Martemyanov, S. M. Morozov, M. Muller-Preussker, and A. I. Veselov, Interrelation between monopoles, vortices, topological

charge and chiral symmetry breaking: Analysis using overlap fermions for SU(2), Phys. Rev. D **77,** 074507 (2008).

[19] A. O'Cais, W. Kamleh, K. Langfeld, B. Lasscock, D. Leinweber, P. Moran, A. Sternbeck, and L. von Smekal, Preconditioning maximal center gauge with stout link smearing in SU(3), Phys. Rev. D **82,** 114512 (2010).

[20] M. Engelhardt, Center vortex model for the infrared sector of SU(3) Yang-Mills theory: Topological susceptibility, Phys. Rev. D **83,** 025015 (2011).

[21] P. O. Bowman, K. Langfeld, D. B. Leinweber, A. Sternbeck, L. von Smekal, and A. G. Williams, Role of center vortices in chiral symmetry breaking in SU(3) gauge theory, Phys. Rev. D **84,** 034501 (2011).

[22] E.-A. O'Malley, W. Kamleh, D. Leinweber, and P. Moran, SU(3) centre vortices underpin confinement and dynamical chiral symmetry breaking, Phys. Rev. D **86,** 054503 (2012).

[23] A. Trewartha, W. Kamleh, and D. Leinweber, Connection between center vortices and instantons through gauge-field smoothing, Phys. Rev. D **92,** 074507 (2015).

[24] J. Greensite, Confinement from center vortices: A review of old and new results, EPJ Web Conf. **137,** 01009 (2017).

[25] J. C. Biddle, W. Kamleh, and D. B. Leinweber, Gluon propagator on a center-vortex background, Phys. Rev. D **98,** 094504 (2018).

[26] F. Spengler, M. Quandt, and H. Reinhardt, Branching of center vortices in SU(3) lattice gauge theory, Phys. Rev. D **98,** 094508 (2018).

[27] J. Biddle, W. Kamleh, and D. Leinweber, Static quark potential from centre vortices in the presence of dynamical fermions, Phys. Rev. D **106,** 054505 (2022).

[28] J. Biddle, W. Kamleh, and D. Leinweber, Impact of dynamical fermions on the centre vortex gluon propagator, Phys. Rev. D **106,** 014506 (2022).

[29] D. Trewartha, W. Kamleh, and D. Leinweber, Evidence that centre vortices underpin dynamical chiral symmetry breaking in SU(3) gauge theory, Phys. Lett. B **747,** 373 (2015).

[30] D. Trewartha, W. Kamleh, and D. B. Leinweber, Centre vortex removal restores chiral symmetry, J. Phys. G **44,** 125002 (2017).

[31] K. Langfeld, Vortex structures in pure SU(3) lattice gauge theory, Phys. Rev. D **69,** 014503 (2004).

[32] J. C. Biddle, W. Kamleh, and D. B. Leinweber, Visualization of center vortex structure, Phys. Rev. D **102,** 034504 (2020).

[33] See Supplemental Material at http://link.aps.org/supplemental/10.1103/PhysRevD.107.094507 contains interactive 3D models of the vortex vacuum, embedded in the text, complementary to the static images presented in the main text. Instructions on how to interact with these models are contained within.

[34] A. Montero, Study of SU(3) vortex—like configurations with a new maximal center gauge fixing method, Phys. Lett. B **467,** 106 (1999).

[35] S. Aoki et al. (PACS-CS Collaboration), 2 + 1 flavor lattice QCD toward the physical point, Phys. Rev. D **79,** 034503 (2009).

[36] Y. Iwasaki, Renormalization group analysis of lattice theories and improved lattice action. II. Four-dimensional non-Abelian SU(N) gauge model, arXiv:1111.7054.

[37] T. G. Kovacs and E. T. Tomboulis, On P vortices and the Gribov problem, Phys. Lett. B **463,** 104 (1999).

[38] V. G. Bornyakov, D. A. Komarov, and M. I. Polikarpov, P vortices and drama of Gribov copies, Phys. Lett. B **497,** 151 (2001).

[39] Advanced Visual Systems, Inc., Avs express, https://www.avs.com/avs-express/ (2020).

[40] West Health Institute, Pyvis, https://github.com/WestHealth/pyvis (2018).

[41] J. L. Hodges, The significance probability of the smirnov two-sample test, Ark. Mat. **3,** 469 (1958).

[42] M. Engelhardt, K. Langfeld, H. Reinhardt, and O. Tennert, Interaction of confining vortices in SU(2) lattice gauge theory, Phys. Lett. B **431,** 141 (1998).

[43] J. Greensite and K. Matsuyama, Confinement criterion for gauge theories with matter fields, Phys. Rev. D **96,** 094510 (2017).

[44] J. Greensite and K. Matsuyama, What symmetry is actually broken in the Higgs phase of a gauge-Higgs theory?, Phys. Rev. D **98,** 074504 (2018).

[45] J. Greensite and K. Matsuyama, Higgs phase as a spin glass and the transition between varieties of confinement, Phys. Rev. D **101,** 054508 (2020).

[46] J. Greensite and K. Matsuyama, Symmetry, confinement, and the Higgs phase, Symmetry **14,** 177 (2022).